

Frozen and β -equilibrated f and p modes of cold neutron stars: nuclear metamodel predictions

Gabriele Montefusco, Marco Antonelli[✉], Francesca Gulminelli[✉]

Université Normandie, ENSICAEN, CNRS/in2p3, LPC-Caen, 14000 Caen, France

E-mail: montefusco@lpccaen.in2p3.fr (G.M.), antonelli@lpccaen.in2p3.fr (M.A.), gulminelli@lpccaen.in2p3.fr (F.G.)

11 October 2024

ABSTRACT

When the chemical re-equilibration timescale is sufficiently long, the normal and quasi-normal mode frequencies of neutron stars should be calculated in the idealized limit that the internal composition of each fluid element is fixed over the oscillation period. However, many studies rely on a barotropic equation of state, which implicitly overlooks potential out-of- β -equilibrium effects. To investigate possible biases arising from this assumption, we calculate the non-radial fundamental (f) and first pressure (p_1) modes for a wide range of neutron star structures, each governed by different nucleonic equations of state. This ensemble is generated using the metamodel technique, a phenomenological framework that incorporates constraints from experimental nuclear physics and chiral effective field theory. The metamodel also provides the internal composition of β -equilibrated $npe\mu$ matter, allowing us to calculate oscillation modes beyond those supported by a purely barotropic fluid. Thus, we systematically assess the impact of assuming a barotropic equation of state across various equations of state and provide a distribution of expected f and p_1 mode frequencies that may be detectable by next-generation gravitational wave interferometers.

1 INTRODUCTION

Neutron stars (NSs) can sustain a variety of oscillation modes due to their stratified internal structure and composition. These normal (or quasi-normal, when the frequency is complex) oscillation modes include fundamental (f), pressure (p), and gravitational (g) modes, among others, each characterized by distinct frequencies and damping times (Thorne & Campolattaro 1967; Reisenegger & Goldreich 1992; Andersson et al. 1996; Kokkotas & Schmidt 1999). A detection of gravitational waves (GWs) emitted by quasi-normal oscillations would allow direct observation of the dominant mode frequencies, enabling a new way of probing NSs internal properties and dynamical processes (Andersson 2021; Jones 2022; Andersson 2019). For example, it has been suggested that the p_1 -mode carries information that can be used to distinguish between nucleonic, hybrid and strange stars (Vásquez Flores & Lugones 2014). To date, forthcoming runs of LIGO, Virgo, Kagra gravitational wave interferometers, and the planned Einstein Telescope and Cosmic Explorer, represent a promising avenue for detecting these oscillations (Andersson et al. 2011; Piccinni 2022; Jones 2022). This holds the appealing prospect of integrating such observations with other data – like results from NICER (Özel et al. 2016) and the planned ATHENA spacecraft (Majczyna et al. 2020) – to constrain the equation of state of dense matter.

Regarding cold NSs, which are the case considered in this work, it is expected that non-radial f -modes can be excited during magnetar flares (Levin & van Hoven 2011; Ball et al. 2024) and

pulsar glitch events (van Eysden & Melatos 2008; Bennett et al. 2010; Ho et al. 2020), see Haskell & Jones (2024) for a recent review and Yim et al. (2024) for an analysis of glitching pulsars candidates as priority targets of future observations. This is an attractive possibility, as future detection of these modes may be used to discriminate between neutron and quark stars (Wilson & Ho 2024; Sotani et al. 2011).

In addition to probing the internal structure of NSs, oscillation modes can be used to disentangle macroscopic characteristics such as mass and radius when used in tandem with other observations. In fact, Andersson & Kokkotas (1998) found a set of quasi-universal relations (QU) – in the sense that they are almost EoS independent relations, see e.g. (Yagi & Yunes 2017) – between the normal mode frequencies and the average density or the compactness. To date, there are numerous studies presenting different QU relations for mode frequencies, usually tested with a small sample of EoSs (Tsui & Leung 2005; Benhar et al. 2004; Pradhan et al. 2022; Sotani 2021), or a large set of purely barotropic (i.e., zero temperature and β -equilibrated) agnostic matter models of the kind used in, e.g., (Lindblom 2010; Breu & Rezzolla 2016; Fasano et al. 2019; Moustakidis et al. 2017; Yao et al. 2024). This poses the motivation for our work. In fact, we will perform a systematic study of proposed QU relations for nucleonic NSs oscillation modes by using a large set of EoSs models that are compatible with the latest astrophysical observations and nuclear physics constraints. This is done by using the phenomenological metamodel technique (Margueron et al. 2018), which allows us to explore the parameter space

of cold $npe\mu$ EoSs and, at the same time, to include the constraints from the chiral effective theory, experimental nuclear physics and astrophysical observations via a Bayesian framework (Zhang et al. 2018; Carreau et al. 2019b; Güven et al. 2020; Dinh Thi et al. 2021a). Furthermore, the metamodel is able to reproduce existing realistic nucleonic models and interpolate between them (Mondal & Gulminelli 2022; Davis et al. 2024).

A downside of exploring a wide parameter space for the metamodel representation of the EoS is that we have to find the f and p_1 mode frequencies for a large set of stellar structures, making it impractical to calculate the frequencies in full General Relativity. Therefore, we have to work within the Cowling approximation, which greatly speeds up the computation of the frequencies. In doing so, we also test the impact of assuming two opposite idealized limits¹ for matter undergoing time-dependent compression, see e.g. (Andersson 2019):

Frozen regime - In this limit the local relaxation processes that bring back $npe\mu$ matter back to β -equilibrium do not have time to occur, as the compression-expansion cycle imparted by the oscillation is faster than the typical reactions mediated by the weak interaction. This limit is characterised by the local conservation of the chemical fractions, meaning that fractions are purely advected by the fluid motion. This is the limit expected to hold in cold NSs (Haensel et al. 2002).

Equilibrium regime - In this limit the relaxation processes are so fast that each fluid element has a negligible departure from β -equilibrium, so that the matter model reduces to the one of a perfect barotropic fluid. Given that the relaxation processes, being mediated by the weak interaction, turn out to be rather slow, this limit is not the relevant one for oscillating cold NSs (Haensel et al. 2002).

Similar to the approach taken for non-compact stars (Hansen & Kawaler 1994), evaluating the mode frequencies requires knowledge of the adiabatic index, which determines how pressure responds to changes in local baryonic density (Thorne & Campolattaro 1967; Shapiro & Teukolsky 1983). The choice of one of the two limits can significantly impact the local value of the adiabatic index and, consequently, the pressure response of $npe\mu$ matter (Haensel et al. 2002; Andersson 2019). Thus, calculating mode frequencies using a barotropic equation of state and a consistent adiabatic index inherently assumes an equilibrium regime.

To investigate the frozen regime, we need an EoS model that is not purely barotropic, allowing the pressure (or adiabatic index) to be calculated at fixed chemical fractions. The metamodel representation of the cold (neutrinoless) $npe\mu$ EoS facilitates the straightforward computation of both the equilibrated and frozen adiabatic indices, enabling a systematic comparison of mode frequencies derived from a purely barotropic EoS versus those that account for the effects of a frozen composition.

In this work, we extend the kind of Bayesian analysis of (Zhang et al. 2018; Carreau et al. 2019b; Güven et al. 2020; Dinh Thi et al. 2021a) by solving, for a large set of metamodel instances, the perturbation equations in the Cowling approximation in the two idealized – frozen and equilibrated – regimes, testing possible deviations from the proposed QU relations. In Sec. 2 we recall the relevant properties the metamodel representation of the energy of cold $npe\mu$

matter. Sec. 3 outlines the Bayesian technique developed for our inference: a large number of metamodel instances are assigned with a likelihood depending on how they satisfy astrophysical and nuclear constraints. Then, in Sec. 4 we summarise how the mode frequencies are obtained for each metamodel instance. Finally, the resulting mode frequencies and their posterior distributions – that may be interpreted as possible frequency range for a future detection – are given in Sec. 5.

2 METAMODEL REPRESENTATION OF THE EQUATION OF STATE AND INTERNAL COMPOSITION

The metamodel representation of the nucleonic EoS of an NS has been introduced in Margueron et al. (2018). The fundamental assumption is that an NS’s core consists of $npe\mu$ matter in weak equilibrium, disregarding the possibility of having other degrees of freedom, albeit it is possible to modify it to account for phase transitions to quark matter (Mondal et al. 2023). The EoS for the uniform $npe\mu$ matter in the core is then consistently prolonged to the lower-density layers of the solid crust thanks to the compressible liquid-drop model approach described in Carreau et al. (2019a); Dinh Thi et al. (2021b). Although not as microscopic as other approaches, this method reproduces results that are consistent with extended Thomas-Fermi calculations at both zero (Grams et al. 2022) and finite temperature (Carreau et al. 2020). Furthermore, it enables quantitative estimation of a unified EoS for both the core and the crust at a relatively low computing cost.

Within the metamodel technique each unified² EoS model is represented by 10 independent empirical parameters which correspond to the coefficients of a 4th order Taylor expansion of the uniform matter binding energy in the isoscalar and isovector channels around saturation density. For non-homogeneous matter, they are supplemented by 5 further surface and curvature parameters (Dinh Thi et al. 2021b), which are however selected by fitting the experimental Atomic Mass Evaluation nuclear mass table (Huang et al. 2021) for each set of the 10 aforementioned parameters. The density dependence of the symmetry energy and the energy in symmetric matter are characterised by these parameters, and over a wide range of nuclear data, their prior distribution is in agreement with current empirical information (Margueron et al. 2018). Three more parameters are needed, two for accounting the density dependence of the effective mass and the effective mass splitting, and one that enforces the correct behavior at zero density, for a total of 13 independent parameters.

As far as this study is concerned, the metamodel can be thought of as a procedure, denoted as \mathcal{M} ,

$$\mathcal{M} : \mathbf{X} \rightarrow \{\epsilon(n_B), P(n_B), \delta(n_B), v_\beta(n_B), v_{FR}(n_B), \dots\} \quad (1)$$

that takes as input the values of 13 nuclear matter parameters \mathbf{X} and outputs a β -equilibrated equation of state (EoS) and the composition of the entire star, including the crust. In practice, \mathcal{M} provides the β -equilibrated total energy density ϵ , pressure P , electron and muon fractions, and nuclear asymmetry δ , all as functions of the baryon number density n_B . We refer to Margueron et al. (2018), Mondal & Gulminelli (2022) and Davis et al. (2024) for an extensive presentation of the nuclear metamodel and its astrophysical

¹ Both limits are non-dissipative, meaning that there is no local entropy generation due to reaction-mediated bulk viscosity; see e.g. (Camelio et al. 2023) or the general discussion in (Gavassino et al. 2021, Sec. II-D).

² I.e., the crust and the core parts of the EoS are built starting from the same nuclear model $\mathcal{M}(\mathbf{X})$ and are matched at a consistent transition density.

applications. Here, we only note that we have added the equilibrated v_β and frozen v_{FR} sound speeds to the metamodel output, which will be important in Sec. 4.

Given non-informative priors on the 13 nuclear matter parameters \mathbf{X} , the resulting metamodel realization³ $\mathcal{M}(\mathbf{X})$ undergoes a Bayesian filtering process that assigns a likelihood $\mathcal{L}(\mathbf{X})$, as in the next section.

3 LIKELIHOOD OF METAMODEL REALIZATIONS

The metamodel instances $\mathcal{M}(\mathbf{X})$ are not all equally realistic, in the sense that some give rise to, say, an EoS that is inconsistent with astrophysical observations, or are not able to reproduce some experimental nuclear phenomenology. Therefore, we assign a likelihood $\mathcal{L}(\mathbf{X})$ to each $\mathcal{M}(\mathbf{X})$ via a sequence of Bayesian filters, similar to the ones detailed in (Dinh Thi et al. 2021a; Davis et al. 2024), see also (Scurto et al. 2024; Malik et al. 2024) for a similar approach with the relativistic mean field:

(i) The nuclear model $\mathcal{M}(\mathbf{X})$ must be consistent with the energy per nucleon of pure neutron matter calculated by chiral effective field theory (χ -EFT) and renormalization group (RG) methods. The conflation of results in the literature obtained from different methods results in an energy band (Huth et al. 2021), which is used to build an informed prior.

(ii) The nuclear model $\mathcal{M}(\mathbf{X})$ must reproduce the nuclear mass measurements in the AME2020 mass table (Huang et al. 2021).

(iii) The β -equilibrated EoS obtained from $\mathcal{M}(\mathbf{X})$ must support a maximum TOV mass greater than that of PSR J0348+0432, as measured by Antoniadis et al. (2013). Additionally, β -equilibrated matter must be stable and causal at least up to the central density of the star with the maximum TOV mass.

(iv) Similarly, we implement the constraint on the tidal deformability from the GW170817 event (Abbott et al. 2019), see App. B.

(v) The mass radius X-ray pulse-profile estimates of the masses and radii of PSR J0030+0451, PSR J0437-4715 and PSR J0740+6620 (Vinciguerra et al. 2024; Choudhury et al. 2024; Salmi et al. 2024).

Compared to the previous Bayesian procedure of Dinh Thi et al. (2021a), the main differences lie in how we implement the causality constraint, which is part of point (iii) and will be discussed later, and how we handle the information from χ -EFT calculations. In fact, we take care of point (i) by constructing a χ -EFT-informed prior via a Metropolis–Hastings sampling, as discussed in Sec. 3.1. Then, we randomly extract 10^5 models $\mathcal{M}(\mathbf{X})$ from this informed prior and pass them through the sequence of Bayesian filters (ii-v), each of which assigns a partial likelihood $\mathcal{L}_i(\mathbf{X})$. The total likelihood of each metamodel instance $\mathcal{M}(\mathbf{X})$ is

$$\mathcal{L}(\mathbf{X}) = \prod_j \mathcal{L}_j(\mathbf{X}) = \prod_j p(D_j | \mathcal{M}(\mathbf{X})) \quad (2)$$

where $p(D_j | \mathcal{M}(\mathbf{X}))$ is the conditional probability of reproducing

³ It may be convenient to identify each metamodel instance $\mathcal{M}(\mathbf{X})$ with the output in (1). While it is true that $\mathcal{L}(\mathbf{X})$ is also the likelihood of the output, $\mathcal{M}(\mathbf{X})$ is actually a phenomenological model for nuclear matter, as it allows to compute more properties than the ones listed in (1).

the data D_j assuming the metamodel instance $\mathcal{M}(\mathbf{X})$, and the index j runs over all the aforementioned constraints. Clearly, $\mathcal{L}(\mathbf{X})$ is automatically also the likelihood of all the stellar properties (e.g., mass-radius relation, mode frequencies) that can be derived by assuming the matter model $\mathcal{M}(\mathbf{X})$.

3.1 Informed Prior from the χ -EFT band

We discuss point (i) above in more detail. State-of-the-art χ -EFT calculations provide the energy per particle $e(n) \pm \delta e(n)$ of pure neutron matter, where $0.02 < n < 0.2 \text{ fm}^{-3}$ is the neutron density and $\delta e(n)$ is the uncertainty associated with the specific calculation. Since different theoretical approaches yield different (overlapping) energy bands $e(n) \pm \delta e(n)$, we combine all the bands presented in (Huth et al. 2021) into a single “conflated” band, where the lower limit is given by the unitary gas approach, see App. A. This ensures that we do not underestimate the uncertainty associated with the theoretical calculations of $e(n)$. Specifically, our conflated band is interpreted as a 90% confidence interval for $e(n)$: for each n , the band is represented by a continuous probability density $p(e|n)$ that is flat within the conflated band and has Gaussian tails accounting for the remaining 5% + 5%, see (A2). This helps achieve a faster burn-in of the Metropolis-Hastings algorithm. Moreover, the Metropolis-Hastings procedure applied to $p(e|n)$ allows us to directly sample the nuclear parameters \mathbf{X} for which $e_{\mathbf{X}}(n)$ obtained from $\mathcal{M}(\mathbf{X})$ lies within our conflated band. This process starts with a flat prior⁴ for the nuclear parameters \mathbf{X} . The resulting posterior is then used as an informed prior for filters (ii-v). This approach provides approximately 10^9 nuclear models $\mathcal{M}(\mathbf{X})$ in the informed prior, which is the most selective yet the least computationally demanding.

3.2 Low density filters from nuclear phenomenology

Each metamodel instance $\mathcal{M}(\mathbf{X})$ can be used to calculate the mass $M_{NZ}(\mathbf{X})$ of a nucleus with N neutrons and Z protons. To do so, a compressible liquid drop model is used, supplemented by 5 extra surface and curvature parameters (Carreau et al. 2019a; Dinh Thi et al. 2021b). Therefore, to implement filter (iii), the idea is to compare the $M_{NZ}(\mathbf{X})$ with the measured nuclear masses M_{NZ}^{AME} listed in the AME2020 mass table (Wang et al. 2021). Following Dinh Thi et al. (2021a), we assign a partial likelihood of zero – i.e., $\mathcal{M}(\mathbf{X})$ is discarded – if it is impossible to find values for the 5 curvature and surface parameters that are consistent with nuclear phenomenology and allow to the nuclear mass table. Otherwise, the partial likelihood is the goodness of the fit:

$$\mathcal{L}_{AME} \propto e^{-\chi(\mathbf{X})^2/2} \quad (3)$$

where the cost function χ^2 is

$$\chi^2(\mathbf{X}) = \frac{1}{N_{AME}} \sum_{NZ} \frac{1}{\sigma_{NZ}^2} \left(M_{NZ}(\mathbf{X}) - M_{NZ}^{AME} \right)^2 \quad (4)$$

where σ_{NZ} is the systematic theoretical error and the label NZ runs over all the N_{AME} nuclei listed in the mass table.

The model distribution after applying filters (i-ii) yields a posterior distribution for the nuclear parameters \mathbf{X} that is consistent with nuclear physics information up to the saturation density. At

⁴ The ranges over which each nuclear parameter can vary are wide enough to be fully consistent with up-to-date nuclear phenomenology (Margueron et al. 2018).

this stage, for every $\mathcal{M}(\mathbf{X})$ that has not been excluded, we can extract the unified β -equilibrated EoS and all relevant outputs in (1) for all layers, including the crust.

3.3 High density filters from astrophysics

Astrophysical constraints are applied through filters (iii-v), which are more sensitive to how $\mathcal{M}(\mathbf{X})$ describes matter above the saturation density. The first check is hard, in the sense that the partial likelihood is either 0 or 1: the Tolman–Oppenheimer–Volkoff (TOV) equations are solved, and the maximum TOV mass $m^*(\mathbf{X})$ is extracted. We assign a unit multiplicative contribution to the total likelihood in (2) for any model that satisfies causality and thermodynamic stability (i.e., $0 < v_\beta^2 < v_{FR}^2 < 1$, see [Camelio et al. 2023](#) for a formal proof), and has a non-negative symmetry energy in the range $0 < n_B < n^*(\mathbf{X})$, where $n^*(\mathbf{X})$ is the central density of the star with mass $m^*(\mathbf{X})$. Otherwise, the model’s likelihood $\mathcal{L}(\mathbf{X})$ is set to zero, i.e. the instance $\mathcal{M}(\mathbf{X})$ is discarded.

After this preliminary hard filter, we can go through the remaining filters (iii-v), which require the mass-radius relation and tidal deformability and are implemented exactly as in ([Dinh Thi et al. 2021a](#); [Scurto et al. 2024](#); [Davis et al. 2024](#)). We briefly list them below and refer to previous work for further details.

To implement filter (iii), we require that the maximum TOV mass $m^*(\mathbf{X})$ exceeds the measured mass of PSR J0348+0432, $M = 2.01 \pm 0.04 M_\odot$ ([Antoniadis et al. 2013](#)). The resulting contribution to the total likelihood is:

$$\mathcal{L}_{J0348} = \frac{1}{0.04\sqrt{2\pi}} \int_0^{m^*(\mathbf{X})/M_\odot} \exp\left(-\frac{(x-2.01)^2}{2 \times 0.04^2}\right) dx \quad (5)$$

Filter (iv) uses data from GW170817 and is based on the comparison between the effective dimensionless tidal deformability $\tilde{\Lambda}$ calculated with $\mathcal{M}(\mathbf{X})$ and the data of the Ligo-Virgo Collaboration (LVC). The likelihood takes the form (see [App. B](#) for details):

$$\mathcal{L}_{LVC} = \int_{0.73}^1 P(\tilde{\Lambda}, q) dq \quad (6)$$

where $\tilde{\Lambda}$ is the effective tidal deformability, $q < 1$ is the mass ratio of the lighter object over the heavier and $P(\tilde{\Lambda}, q)$ is the observational joint posterior distribution reported in ([Abbott et al. 2019](#)).

Finally, in filter (v) we check if the mass-radius relation $R_{\mathbf{X}}(m)$ obtained with the nuclear model $\mathcal{M}(\mathbf{X})$ is consistent with the updated NICER estimates of the joint mass-radius distributions for three pulsars:

$$\mathcal{L}_{NICER} = \prod_{i=1,2,3} \int_{0.7M_\odot}^{m^*(\mathbf{X})} P_i(m, R_{\mathbf{X}}(m)) dm \quad (7)$$

where P_1 is the joint probability distribution of mass and radius of the PSR J0030+0451 pulsar ([Vinciguerra et al. 2024](#)), P_2 refers to PSR J0437-4715 ([Choudhury et al. 2024](#)) and P_3 to PSR J0740+6620 ([Salmi et al. 2024](#)).

4 FROZEN AND EQUILIBRATED NORMAL MODES

The Bayesian procedure outlined in the previous section allows us to assign a likelihood to each model $\mathcal{M}(\mathbf{X})$ based on its compatibility with nuclear physics phenomenology and astrophysical constraints. We now proceed to compute the normal mode frequencies, with the double aim of checking the impact of chemical transmutation and obtaining a posterior predictive distribution based on $\mathcal{L}(\mathbf{X})$ for the mode frequencies.

First, we recall how to determine the frequencies of the f and p_1 normal modes of a spherically symmetric non-rotating NS in the relativistic Cowling approximation ([McDermott et al. 1983](#)). Since the spacetime remains unperturbed, no gravitational waves are emitted and, consequently, the radiation damping is absent. Moreover, the two equilibrated and frozen limits we consider are non-dissipative regimes (e.g. [Gavassino et al. 2021](#), Sec. II-D), implying that there is no bulk viscosity damping due to reactions (e.g. [Sawyer 1989](#); [Haensel et al. 2002](#); [Alford & Harris 2019](#); [Alford et al. 2023](#)). This limits our study to purely real frequencies. Following [Sotani et al. \(2011\)](#), the spherical spacetime metric is

$$ds^2 = -e^{2\Phi} dt^2 + e^{2\Lambda} dr^2 + r^2 d\theta^2 + r^2 \sin^2 \theta d\phi^2, \quad (8)$$

while the Lagrangian fluid displacements vector is

$$\xi^i = r^{-2} \left(\tilde{W} e^{-\Lambda} Y_{lm}, -\tilde{V} \partial_\theta Y_{lm}, -\tilde{V} \sin^{-2} \theta \partial_\phi Y_{lm} \right) \quad (9)$$

where $\tilde{W}(r, t) = W(r)e^{i\omega t}$ and $\tilde{V}(r, t) = V(r)e^{i\omega t}$ characterize the amplitude of the perturbation and Y_{lm} are the spherical harmonics. Using these variables, the equations for the oscillation modes are

$$\begin{aligned} \frac{dW}{dr} &= \left(\frac{dP}{d\epsilon} \right)^{-1} \left[\omega^2 r^2 e^{\Lambda-2\Phi} V + \frac{d\Phi}{dr} W \right] - l(l+1) e^\Lambda V \\ \frac{dV}{dr} &= 2 \frac{d\Phi}{dr} V - \frac{1}{r^2} e^\Lambda W \end{aligned} \quad (10)$$

The different regime of the balance between oscillations frequency and reaction rate is determined by the term $dP/d\epsilon$, the squared speed of sound, which encodes information equivalent to the one in the adiabatic index (e.g. [Haensel et al. 2002](#); [Andersson 2019](#)).

Boundary conditions at the star center and surface are required to solve the system in (10). Inspection of the system shows that $W(r) = Cr^{l+1} + \mathcal{O}(r^{l+3})$ and $V(r) = Cr^l + \mathcal{O}(r^{l+2})$ for $r \rightarrow 0$, with C being an arbitrary constant. The other boundary condition is obtained by demanding that the pressure perturbation vanishes at the stellar surface, which leads to

$$\omega^2 r^2 e^{\Lambda-2\Phi} V + \frac{d\Phi}{dr} W = 0 \quad (11)$$

With this condition, the problem becomes an eigenvalue problem, which we solve using a standard shooting method. After determining the metric functions and stellar structure by solving the TOV equations, we solve the system in (10) using an initial guess for the (purely real and positive) pulsation ω . We then refine the value of ω with a bisection method, iterating the process until we find the exact ω that satisfies (11).

4.1 Frozen speed of sound and thermodynamic stability-causality condition

For perturbations that are slow enough, matter will be always almost in β -equilibrium and $dP/d\epsilon$ in (10) can be taken to be v_β^2 , the sound speed arising from a purely barotropic EoS:

$$\frac{dP}{d\epsilon} = \frac{dP(n_B, \delta(n_B))/dn_B}{d\epsilon(n_B, \delta(n_B))/dn_B} = v_\beta^2 \quad (12)$$

On the other hand, in a fast oscillation regime the composition of each fluid element has no time to relax back to chemical equilibrium and one should use the sound speed v_{FR}^2 at frozen composition, that we conveniently write as

$$\left. \frac{\partial P}{\partial \epsilon} \right|_{\delta(n_B)} = \frac{\partial P(n_B, \delta(n_B))/\partial n_B}{\partial \epsilon(n_B, \delta(n_B))/\partial n_B} = v_{FR}^2 \quad (13)$$

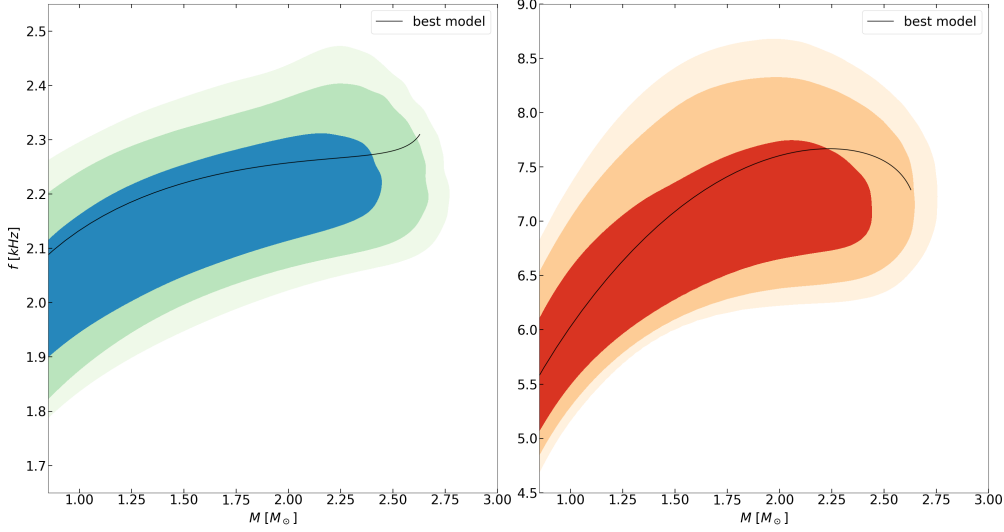


Figure 1. Probability density distributions for the f -mode frequencies (left) and the p_1 -mode (right), both obtained within the Cowling approximation in the barotropic limit. The three shaded regions refer to the 68%, 95%, and 99% percentiles. The black solid line represent the model with the highest likelihood.

For a thermodynamically stable and causal⁵ matter model, it is possible to show that $0 < v_{\beta}^2 < v_{FR}^2 < 1$, where v_{FR} is the actual speed of a signal propagating in a chemically reacting fluid mixture (see Sec. V of [Camelio et al. 2023](#)). From the point of view of global oscillations, in particular g -modes (e.g. [Lai 1994](#); [Jaikumar et al. 2021](#); [Tran et al. 2023a](#)), the same criterion guarantees local the convective stability of the star, cf. equation (A12) of [Camelio et al. \(2023\)](#) with equation (4.17) in [Lai \(1994\)](#). Therefore, as mentioned in Sec. 3.3, we retain only the metamodel instances $\mathcal{M}(\mathbf{X})$ that satisfy the fundamental thermodynamics stability-causality condition $0 < v_{\beta}^2(n_B) < v_{FR}^2(n_B) < 1$ at least up to the central density of the NS with maximum TOV mass.

5 RESULTS AND DISCUSSION

For each nuclear model $\mathcal{M}(\mathbf{X})$, we extract the f and p_1 normal mode frequencies in the Cowling approximation, with the purpose of testing the QU relations with a large set of metamodel instances and quantifying the potential impact of assuming frozen or equilibrated composition. Finally, we use the known QU relation in full General Relativity to estimate a more realistic posterior predictive distribution for the mode frequencies.

5.1 Differences between frozen and beta-equilibrated frequencies

We have evaluated the Cowling frequencies of the f and p_1 -modes in the two ideal limits of frozen and equilibrated composition, as outlined in the previous section. The results are shown in Fig. 1. The frequencies of the f -mode are almost unaffected by the equilibration assumption, with differences smaller than 0.5%. On the other hand, the p_1 -mode exhibits a more interesting behaviour, where the

difference between the two cases are more evident and tend to increase with mass, as can be seen in Fig. 2. For the models with high likelihood, the ones in the darkest region of the plot, the frequencies calculated in the frozen limit remain close to the ones obtained by assuming the barotropic sound speed.

Given these results, we present only the frozen frequencies in the following discussion, as the differences are negligible for the f -mode and less than 5% for the p_1 -mode in reasonable mass ranges (not too close to the maximum TOV mass). For the same reason, the present analysis confirms – on the basis of a large set of nuclear models – that when the frozen speed of sound or the frozen adiabatic index is unavailable, the β -equilibrated speed of sound v_{β} can be used with minimal error. Namely, f and p_1 modes obtained with agnostic barotropic models can be trusted with the 5% or better, especially for masses below $\sim 2M_{\odot}$.

5.2 Test of proposed quasi-universal relations

[Andersson & Kokkotas \(1998\)](#) proposed a QU relation for the p_1 -mode, where the mode pulsation ω times the NS mass M was expressed in terms of the compactness M/R . This same scaling was later used to look for a QU relation for the f -mode by [Tsui & Leung \(2005\)](#):

$$\omega M \text{ (rad/s km)} = a_3 \left(\frac{M}{R}\right)^3 + a_2 \left(\frac{M}{R}\right)^2 + a_1 \frac{M}{R} + a_0, \quad (14)$$

where the coefficients a_i are obtained from a fit over a limited number of barotropic EoS models. This empirical expression has been recently tested with $a_2 = a_3 = 0$ for the f -mode in the Cowling approximation ([Pradhan & Chatterjee 2021](#)) and with $a_3 = 0$ for the f -mode in full General Relativity ([Pradhan et al. 2022](#)). Moreover, [Sotani \(2021\)](#) applied the empirical relation (14), including all coefficients, to the p_1 -mode frequencies in full GR (see Tab. 1).

As a preliminary check, we evaluated the accuracy of the QU relation (14) using our set of metamodel instances, in order to assess the quality of the proposed fits and the dispersion of the metamodel instances around them. The results are presented in Fig. 3, where we compare our findings with the fits from the aforementioned works (the coefficients of these fits are listed in Tab. 1, along with a fit of the

⁵ The full thermodynamic equilibrium state is stable against fluctuations and matter perturbations remain within their light-cone envelope, see e.g. ([Olson & Hiscock 1989](#); [Gavassino et al. 2022](#)).

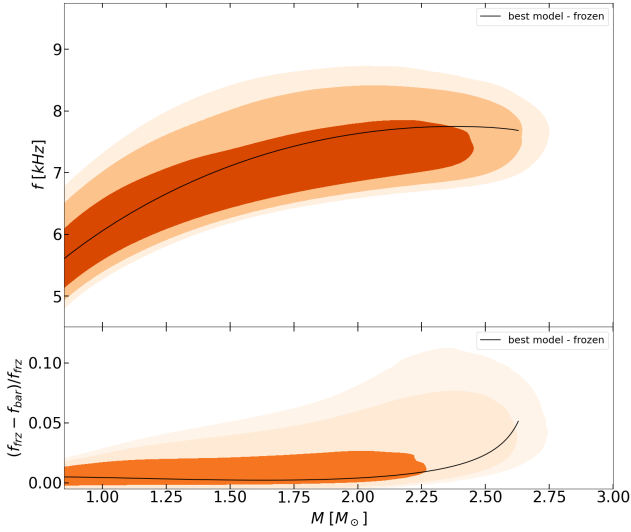


Figure 2. Posterior probability density for the frequencies of the frozen p_1 -mode (upper panel). The lower panel illustrates the difference between the frequencies in the frozen limit and those in the barotropic limit. The three shaded regions correspond to the 68%, 95%, and 99% percentiles, while the black line represents the model with the highest likelihood.

p_1 -mode to our numerical results). The first panel of Fig. 3 shows the density map of mode frequencies resulting from our Bayesian filtering, with the f -mode in blue-green and the p_1 -mode in orange-yellow, alongside the various QU relations mentioned earlier. The two lower panels show the differences between the models and the Cowling relations, which measure the dispersion of the metamodel instances around the QU fits.

In both panels of Fig. 3, the dispersion around the proposed f -mode QU fit is minimal, demonstrating that our large set of phenomenological EoSs follows it to the expected degree of precision, with errors smaller than 2.5%. However, a structure in the residuals remains visible, which can be attributed to the choice of a linear fit. In contrast, the functional form for the fit of the p_1 -mode QU seems appropriate, as there are no evident underlying structures observed in the dispersion of the residuals. Nevertheless, it is noteworthy that in this case the precision to which the QU relation is realised is lower, with errors ranging from approximately 5% to 10%.

For completeness, we have also tested an alternative empirical relation, linking the f -mode frequency and the average density of the star (Andersson & Kokkotas 1998; Pradhan et al. 2022):

$$f = a + b \left(\frac{\bar{M}}{\bar{R}^3} \right)^{1/2} \quad (15)$$

where $\bar{M} = M/1.4M_\odot$, $\bar{R} = R/10 \text{ km}$ and the constants a and b are obtained from a fit to the numerical results. This relation has been tested by different authors with different barotropic EoS (not all compatible with the constraint imposed by the measured mass of PSR J0348+0432). Therefore, we verify whether (15) is a QU relation by using our filtered set of nuclear models. This is shown in Fig. 5.2: the upper distribution represents our Cowling results, which is compared to the one obtained by reversing relation (14) with the coefficients provided in Pradhan et al. (2022). We also compare these distributions to the empirical relations presented in Pradhan et al. (2022), Benhar et al. (2004), and Andersson & Kokkotas (1998). Since these empirical relations are all derived from fits to frequencies extracted in full GR, they are obviously

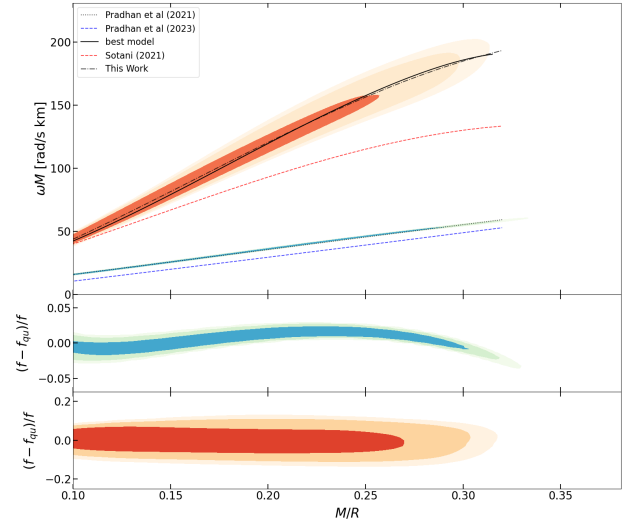


Figure 3. Relationship between the rescaled pulsations ωM and the compactness M/R for the frozen f -modes (blue-green) and frozen p_1 -modes (orange-yellow). The dashed lines correspond to the fits presented in Tab. 1, while the black solid line represents the model $\mathcal{M}(\mathbf{X})$ with the highest likelihood $\mathcal{L}(\mathbf{X})$. The fit lines overlapping with the distributions are based on the Cowling approximation, whereas the others, obtained in full GR, are shown for comparison. The differences between the rescaled pulsations ωM calculated in the Cowling approximation and the corresponding QU fits are illustrated in the two lower panels. Each panel also includes three shaded regions representing the 68%, 95%, and 99% quantiles of the distribution.

not compatible with our Cowling results. In contrast, the Cowling relation presented in Pradhan & Chatterjee (2021), obtained within the Cowling approximation, shows compatibility with our results. The values of the coefficients a and b for all the fits can be found in Table II of Pradhan et al. (2022). It can be observed that this relation strongly depends on the selected set of EoS, indicating that it cannot be classified as quasi-universal.

5.3 Synthetic full GR mode frequencies

The QU relation in (14) can be used to quickly estimate the frequencies for $\mathcal{M}(\mathbf{X})$ in full GR directly from the $R_{\mathbf{X}}(M)$ relation, as long as the opportune parameters a_i are used. Together with the likelihood $\mathcal{L}(\mathbf{X})$, we use the mass-radius relations $R_{\mathbf{X}}(M)$ to extract a posterior predictive for the mode frequencies of the f and p_1 -mode beyond the Cowling approximation. We will denote these frequencies as “synthetic” since they are not obtained by solving the eigenvalue problem but rather simply by unpacking the QU relation (14) via the mass-radius relation $R_{\mathbf{X}}(M)$ of each $\mathcal{M}(\mathbf{X})$.

More precisely, the procedure used to recover the synthetic frequencies f_{GR} in full GR (i.e., beyond the Cowling approximation) is:

$$f_{GR}(M) = \frac{1 + \Delta(M)}{2\pi M} U_{GR}(M) \quad (16)$$

with Δ given by

$$\Delta(M) = \frac{M \omega_C(M) - U_C(M)}{U_C(M)} \quad (17)$$

where ω_C is the mode pulsation that we found within the Cowling approximation in the frozen limit; $U_{C,GR}$ is the Cowling (C) or full GR (GR) quasi-universal relation, namely the right hand side of (14) with the appropriate coefficients a_i listed in Tab. 1.

Reference	QU	a_0	a_1	a_2	a_3
Pradhan & Chatterjee (2021)	eq. (29), Cowling f -mode	-3.84	197.30	0	0
Pradhan et al. (2022)	eq. (33), full GR f -mode	-7.16	165.07	21.77	0
Sotani (2021)	eq. (16), full GR p_1 -mode	-3.74	307.168	1724.9	-4201.2
This Work	eq. (14), Cowling p_1 -mode	-10.61	317.34	2844.4	-5762.5

Table 1. Coefficients a_i of the QU relations shown in Fig. 3.

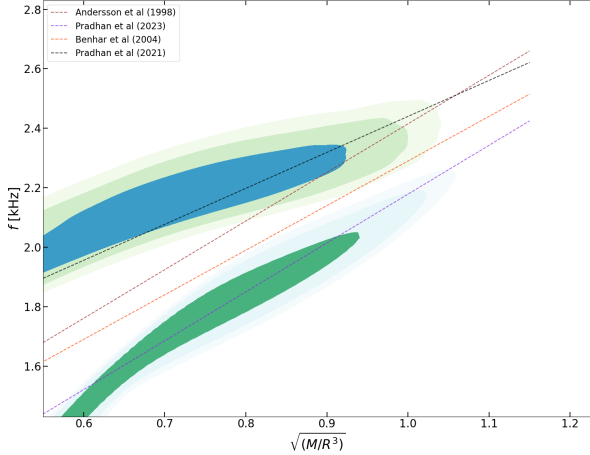


Figure 4. Distributions of the f -mode frequencies as a function of the average density \bar{M}/\bar{R}^3 . The upper color map refers to the frequencies we obtain within the Cowling approximation, while the lower distribution is obtained by reversing the relation in (14) with the coefficients a_i from Pradhan et al. (2022). For comparison, the lines are the several fits listed in Tab-II of Pradhan et al. (2022). The three shaded regions contain the 68%, 95%, and 99% quantiles of the distribution.

The prescription (16) for the synthetic frequencies f_{GR} is designed so that we do not underestimate the spread of the p_1 frequencies, as discussed in App. C. Essentially, we unpack the QU relation in (14), with the coefficients a_i extracted from numerical results in full GR, and transporting the spread of our Cowling calculation onto the unpacked results.

Fig. 5.3 shows the probability density of the frequencies for the f -mode and p_1 -mode. As expected, the f -mode frequency increases more rapidly with mass than the p_1 -mode, which remains relatively flat. Consequently, extrapolating NS features from the p_1 -mode frequencies is expected to be much more challenging. To quantify this further, in Fig. 5.3 we show the posterior distributions of frequencies for an NS with masses of $M = 1M_\odot, 1.4M_\odot, 2M_\odot$ in the frozen limit. The three distributions for the p_1 -mode are nearly indistinguishable, as they almost completely overlap. In contrast, the three distributions for the f -mode show only partial overlap, suggesting that it may be possible to constrain the mass of an NS despite uncertainties in the nuclear EoS.

6 CONCLUSIONS

With the advent of next-generation interferometers, it becomes important to evaluate how future GW detection from oscillating NSs could be used to constrain nuclear models of neutron star interiors or infer the mass of the object. To address this, we adopted the nuclear metamodel framework (Margueron et al. 2018) for cold $npe\mu$ matter, generating a large set of unified equations of state, together

with their β -equilibrated composition and the two (barotropic and frozen) sound speeds. These nuclear models were then assigned likelihoods $\mathcal{L}(\mathbf{X})$ through a sequence of Bayesian filters, designed to weight each metamodel instance based on its consistency with established nuclear and astrophysical phenomena. Given this posterior for the EoSs, we find the posterior predictive distributions for the f and p_1 mode frequencies – shown in Fig. 5.3 – by inverting known full GR quasi-universal relations. More precisely, Fig. 5.3 is our “synthetic” full GR prediction of the f and p_1 mode frequencies as a function of the NS’s mass: while an f -mode detection could constrain the NS mass, this information is almost completely lost for the p_1 mode.

The generation of a large set of metamodel instances and the relative stellar structures for different masses also allowed us to check another point, that is more related to the physical assumptions underlying the computation of the modes. Proposed QU relations pertaining to mode frequencies have been found by using barotropic models or, equivalently, non-barotropic nuclear models always at strict β -equilibrium, namely using $dP/d\epsilon = v_\beta^2$ in (10). Hence, we checked the impact of the, more realistic (Haensel et al. 2002), frozen limit assumption $dP/d\epsilon = v_{FR}^2$, to see if it could introduce any deviation from the known QU relations for the f and p_1 modes. This check is a first, albeit partial, step towards a more systematic study of the effect of reactions in quasi-normal modes: in principle, reactions introduce mode damping, which strength depends on the details of the nuclear model and physical conditions of temperature and density (e.g. Haensel et al. 2002; Alford & Harris 2019; Alford et al. 2023, 2024). However, in the two ideal limits considered here, any possible bulk-viscous effect is exactly zero (Gavassino et al. 2021; Camelio et al. 2023). This is a caveat to be kept in mind.

Our analysis shows that both the f and p_1 modes do not significantly depend on whether the sound speed used is the barotropic or frozen one. This is in contrast with what is known for g -modes, where both velocities have to be used to find the frequency spectrum (e.g., Reisenegger & Goldreich 1992; Tran et al. 2023b; Zhao & Lattimer 2022). Therefore, we conclude that studies assuming purely barotropic agnostic models for the EoS are accurate within a few percent. This behavior is reflected in the goodness of the QU relation, which can thus be used to estimate the mode frequencies without solving the perturbation equations. This is crucial in Bayesian studies, where millions of agnostic EoSs are employed.

7 ACKNOWLEDGEMENTS

We thank Hoa Dinh Thi, Micaela Oertel, Chiranjib Mondal and Debarati Chatterjee for useful discussion, and Philip John Davis for technical support. Partial support comes from the IN2P3 Master Project NewMAC, the ANR project “Gravitational waves from hot neutron stars and properties of ultra-dense matter” (GW-HNS, ANR-22-CE31-0001-01), and the CNRS International Research

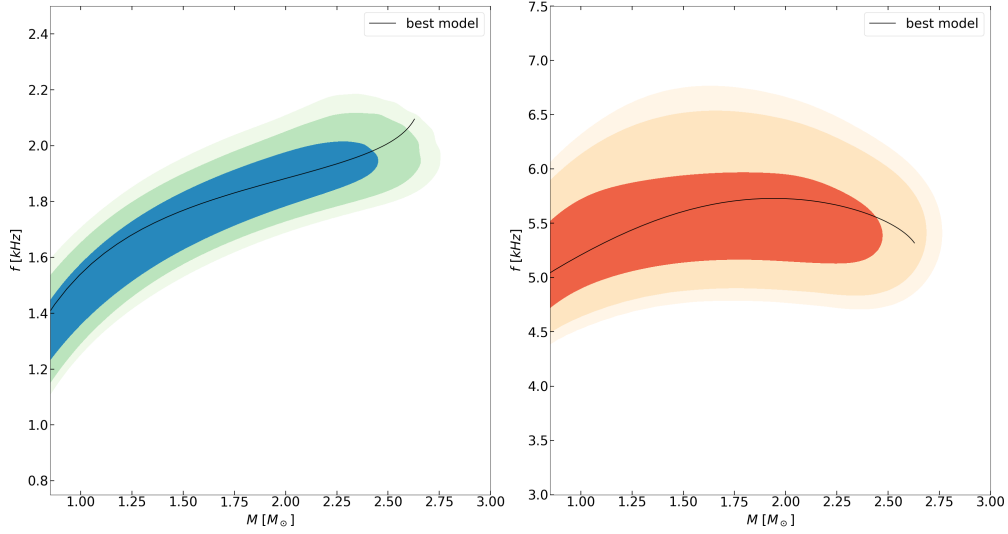


Figure 5. Probability distributions of the synthetic full GR frequencies obtained from (16). The left panel shows the f -mode while the right one the p_1 -mode. The three shaded regions in each panel contain the 68%, 95%, and 99% percentiles.

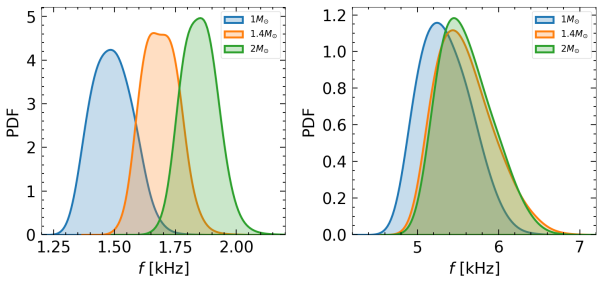


Figure 6. Distribution of the synthetic full GR frequencies at $1M_{\odot}$, $1.4M_{\odot}$ and $2M_{\odot}$ obtained from (16). The left panel refers to the f -mode while the right one to the p_1 -mode.

Project (IRP) “Origine des éléments lourds dans l’univers: Astres Compacts et Nucléosynthèse” (ACNu).

8 DATA AVAILABILITY

The data used in this article are cited accordingly in the main text. The numerical results and the code underlying this work are available from the authors, upon reasonable request. No new observational data were generated in support of this research.

REFERENCES

Abbott B. P., et al., 2019, *Physical Review X*, **9**, 011001
 Alford M. G., Harris S. P., 2019, *Phys. Rev. C*, **100**, 035803
 Alford M., Harutyunyan A., Sedrakian A., 2023, *Phys. Rev. D*, **108**, 083019
 Alford M. G., Haber A., Zhang Z., 2024, *Phys. Rev. C*, **109**, 055803
 Andersson N., 2019, Gravitational-Wave Astronomy: Exploring the Dark Side of the Universe, doi:10.1093/oso/9780198568032.001.0001/oso-9780198568032.
 Andersson N., 2021, *Universe*, **7**, 97
 Andersson N., Kokkotas K. D., 1998, *MNRAS*, **299**, 1059
 Andersson N., Kojima Y., Kokkotas K. D., 1996, *ApJ*, **462**, 855
 Andersson N., Ferrari V., Jones D. I., Kokkotas K. D., Krishnan B., Read

J. S., Rezzolla L., Zink B., 2011, *General Relativity and Gravitation*, **43**, 409
 Antoniadis J., et al., 2013, *Science*, **340**, 448
 Ball M., Frey R., Merfeld K., 2024, *MNRAS*, **533**, 3090
 Benhar O., Ferrari V., Gualtieri L., 2004, *Phys. Rev. D*, **70**, 124015
 Bennett M. F., van Eysden C. A., Melatos A., 2010, *MNRAS*, **409**, 1705
 Breu C., Rezzolla L., 2016, *MNRAS*, **459**, 646
 Camelio G., Gavassino L., Antonelli M., Bernuzzi S., Haskell B., 2023, *Phys. Rev. D*, **107**, 103031
 Carreau T., Gulminelli F., Margueron J., 2019a, *European Physical Journal A*, **55**, 188
 Carreau T., Gulminelli F., Margueron J., 2019b, *Phys. Rev. C*, **100**, 055803
 Carreau T., Gulminelli F., Chamel N., Fantina A. F., Pearson J. M., 2020, *A&A*, **635**, A84
 Choudhury D., et al., 2024, *ApJ*, **971**, L20
 Davis P. J., Dinh Thi H., Fantina A. F., Gulminelli F., Oertel M., Suleiman L., 2024, *A&A*, **687**, A44
 Dinh Thi H., Mondal C., Gulminelli F., 2021a, *Universe*, **7**, 373
 Dinh Thi H., Carreau T., Fantina A. F., Gulminelli F., 2021b, *A&A*, **654**, A114
 Fasano M., Abdelsalhin T., Maselli A., Ferrari V., 2019, *Phys. Rev. Lett.*, **123**, 141101
 Gavassino L., Antonelli M., Haskell B., 2021, *Classical and Quantum Gravity*, **38**, 075001
 Gavassino L., Antonelli M., Haskell B., 2022, *Phys. Rev. Lett.*, **128**, 010606
 Grams G., Somasundaram R., Margueron J., Reddy S., 2022, *Phys. Rev. C*, **105**, 035806
 Güven H., Bozkurt K., Khan E., Margueron J., 2020, *Phys. Rev. C*, **102**, 015805
 Haensel P., Levenfish K. P., Yakovlev D. G., 2002, *A&A*, **394**, 213
 Hansen C. J., Kawaler S. D., 1994, *Stellar Interiors. Physical Principles, Structure, and Evolution.*, doi:10.1007/978-1-4419-9110-2.
 Haskell B., Jones D. I., 2024, *Astroparticle Physics*, **157**, 102921
 Ho W. C. G., Jones D. I., Andersson N., Espinoza C. M., 2020, *Phys. Rev. D*, **101**, 103009
 Huang W. J., Wang M., Kondev F. G., Audi G., Naimi S., 2021, *Chinese Physics C*, **45**, 030002
 Huth S., Wellenhofer C., Schwenk A., 2021, *Phys. Rev. C*, **103**, 025803
 Jaikumar P., Semposki A., Prakash M., Constantinou C., 2021, *Phys. Rev. D*, **103**, 123009
 Jones D. I., 2022, in , *Astrophysics in the XXI Century with Compact Stars*. Edited by C.A.Z. Vasconcellos. eISBN 978-981-12-2094-4. Singapore: World Scientific. pp 201–217, doi:10.1142/9789811220944_0006

- Kokkotas K. D., Schmidt B. G., 1999, *Living Reviews in Relativity*, **2**, 2
- Lai D., 1994, *MNRAS*, **270**, 611
- Levin Y., van Hoven M., 2011, *Mon. Not. Roy. Astron. Soc.*, **418**, 659
- Lindblom L., 2010, *Phys. Rev. D*, **82**, 103011
- Majczyna A., Madej J., Należyty M., Różańska A., Beldycki B., 2020, *ApJ*, **888**, 123
- Malik T., Dexheimer V., Providência C., 2024, *Phys. Rev. D*, **110**, 043042
- Margueron J., Hoffmann Casali R., Gulminelli F., 2018, *Phys. Rev. C*, **97**, 025805
- McDermott P. N., van Horn H. M., Scholl J. F., 1983, *ApJ*, **268**, 837
- Mondal C., Gulminelli F., 2022, *Phys. Rev. D*, **105**, 083016
- Mondal C., Antonelli M., Gulminelli F., Mancini M., Novak J., Oertel M., 2023, *MNRAS*, **524**, 3464
- Moustakidis C. C., Gaitanos T., Margaritis C., Lalazissis G. A., 2017, *Phys. Rev. C*, **95**, 045801
- Olson T. S., Hiscock W. A., 1989, *Phys. Rev. C*, **39**, 1818
- Özel F., Psaltis D., Arzumianian Z., Morsink S., Bauböck M., 2016, *ApJ*, **832**, 92
- Piccinni O. J., 2022, *Galaxies*, **10**, 72
- Pradhan B. K., Chatterjee D., 2021, *Phys. Rev. C*, **103**, 035810
- Pradhan B. K., Chatterjee D., Lanoye M., Jaikumar P., 2022, *Phys. Rev. C*, **106**, 015805
- Reisenegger A., Goldreich P., 1992, *ApJ*, **395**, 240
- Salmi T., et al., 2024, *arXiv e-prints*, p. arXiv:2406.14466
- Sawyer R. F., 1989, *Phys. Rev. D*, **39**, 3804
- Scurto L., Pais H., Gulminelli F., 2024, *Phys. Rev. D*, **109**, 103015
- Shapiro S. L., Teukolsky S. A., 1983, Black holes, white dwarfs and neutron stars. The physics of compact objects, doi:10.1002/9783527617661.
- Shen H., Toki H., Oyamatsu K., Sumiyoshi K., 1998, *Nuclear Phys. A*, **637**, 435
- Sotani H., 2021, *Phys. Rev. D*, **103**, 123015
- Sotani H., Yasutake N., Maruyama T., Tatsumi T., 2011, *Phys. Rev. D*, **83**, 024014
- Thorne K. S., Campolattaro A., 1967, Non-Radial Pulsation of General-Relativistic Stellar Models. I. Analytic Analysis for $L \geq 2$, doi:10.1086/149288
- Tran V., Ghosh S., Lozano N., Chatterjee D., Jaikumar P., 2023a, *Phys. Rev. C*, **108**, 015803
- Tran V., Ghosh S., Lozano N., Chatterjee D., Jaikumar P., 2023b, *Phys. Rev. C*, **108**, 015803
- Tsui L. K., Leung P. T., 2005, *MNRAS*, **357**, 1029
- Vásquez Flores C., Lugones G., 2014, *Classical and Quantum Gravity*, **31**, 155002
- Vinciguerra S., et al., 2024, *ApJ*, **961**, 62
- Wang M., Huang W., Kondev F., Audi G., Naimi S., 2021, *Chinese Physics C*, **45**, 030003
- Wilson O. H., Ho W. C. G., 2024, *Phys. Rev. D*, **109**, 083006
- Yagi K., Yunes N., 2017, *Phys. Rep.*, **681**, 1
- Yao N., Sorensen A., Dexheimer V., Noronha-Hostler J., 2024, *Phys. Rev. C*, **109**, 065803
- Yim G., Shao L., Xu R., 2024, *MNRAS*,
- Zhang N.-B., Li B.-A., Xu J., 2018, *ApJ*, **859**, 90
- Zhao T., Lattimer J. M., 2022, *Phys. Rev. D*, **106**, 123002
- van Eysden C. A., Melatos A., 2008, *Classical and Quantum Gravity*, **25**, 225020

APPENDIX A: THE CHIRAL BAND FOR PURE NEUTRON MATTER

The χ -EFT ab-initio calculations taken into account in this work are presented in Fig. 1 of Huth et al. (2021): the i -th approach provides an estimate of $e_i(n) \pm \delta e_i(n)$, the energy per baryon of pure neutron matter in the range $0.02 < n < 0.2 fm^{-3}$ where all approaches are expected to provide reliable results. For each meta-model instance $\mathcal{M}(\mathbf{X})$, we can easily extract $e_{\mathbf{X}}(n)$, and compare it with the theoretical microscopic results $e_i(n) \pm \delta e_i(n)$. To this

end, we have to conflate all the bands $e_i(n) \pm \delta e_i(n)$ reported in Huth et al. (2021) into a single one, $e(n) \pm \delta e(n)$: the lower limit $e_-(n) = e(n) - \delta e(n)$ is given by the unitary gas model, while the upper bound $e_+(n) = e(n) + \delta e(n)$ is

$$e_+(n) = \max_i \{e_i(n) + \delta e_i(n)\} \quad (\text{A1})$$

In order not to underestimate the theoretical systematic error, we interpret $[e_-(n), e_+(n)]$ as the the 90% confidence interval where $e_{\mathbf{X}}(n)$ should lie arising from a smooth probability distribution to be used within the metropolis-Hastings algorithm. Namely, we consider the following normalized distribution:

$$p(e|n) = Q_n \begin{cases} \exp\left(-\frac{(e-e_-(n))^2}{2\sigma_n^2}\right) & \text{if } e \in (-\infty, e_-(n)] \\ 1 & \text{if } e \in (e_-(n), e_+(n)] \\ \exp\left(-\frac{(e-e_+(n))^2}{2\sigma_n^2}\right) & \text{if } e \in (e_+(n), \infty) \end{cases} \quad (\text{A2})$$

where

$$Q_n = \frac{0.9}{e_+(n) - e_-(n)} \quad \sigma_n = \frac{e_+(n) - e_-(n)}{9\sqrt{2\pi}} \quad (\text{A3})$$

In this way, the central plateau of the distribution accounts for the 90% while each tail for the remaining 10%, in accordance with other prescriptions used previous studies (Dinh Thi et al. 2021a; Carreau et al. 2019a; Scurto et al. 2024). Then, the partial likelihood of $\mathcal{M}(\mathbf{X})$ is given by the geometric product integral

$$\mathcal{L}_{\chi EFT}(\mathbf{X}) = \exp \int dn \log p(e|n) \quad (\text{A4})$$

over the $0.02 < n < 0.2 fm^{-3}$ density range. In practice, the density range is divided in N equally spaced slices at densities n_j and the resulting likelihood is

$$\mathcal{L}_{\chi EFT}(\mathbf{X}) \propto \prod_{j=1}^N p(e_{\mathbf{X}}(n_j) | n_j) \quad (\text{A5})$$

APPENDIX B: SCHEME FOR THE LVC CONSTRAINT

We provide a schematic presentation of the LVC constraint in (6). This may help the reader to sort the details and complement the presentation given in previous works that adopt the exact same prescription (Dinh Thi et al. 2021a; Mondal & Gulminelli 2022; Scurto et al. 2024; Davis et al. 2024).

The analysis in Abbott et al. (2019) provides the observational joint posterior $P(\tilde{\Lambda}, q)$ for the effective tidal deformability $\tilde{\Lambda}$ and the mass ratio q of GW170817. In principle, both quantities can be determined from the masses m_k and tidal deformabilities Λ_k of the two NSs ($k = 1, 2$) using known analytical expressions, $\tilde{\Lambda}(m_k, \Lambda_k)$ and $q(m_k)$. The GW170817 data enabled a relatively precise determination of the chirp mass m_c (treated as a given constant in the following), which can also be expressed analytically in terms of the two masses, $m_c(m_k)$.

To implement the constraint imposed by knowledge of $P(\tilde{\Lambda}, q)$ and m_c , the first step is to recognize that we are adopting a framework where the mass M is treated as an independent variable, and $\mathcal{M}(\mathbf{X})$ can be used to obtain the relations $R_{\mathbf{X}}(M)$ and $\Lambda_{\mathbf{X}}(M)$. This is a natural and convenient choice, considering that $R_{\mathbf{X}}(M)$ and $\Lambda_{\mathbf{X}}(M)$ are genuine functions, whereas $M_{\mathbf{X}}(R)$ or $\Lambda_{\mathbf{X}}(R)$ could be multivalued.

Now, the observational information we have is $P(\tilde{\Lambda}, q)$ and the value of m_c , but both q and m_c depend only on the masses that, in our framework, carry no dependence on $\mathcal{M}(\mathbf{X})$. Therefore, the

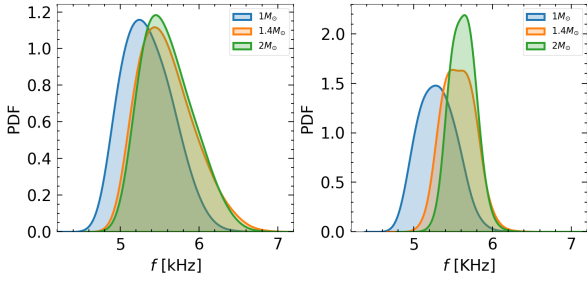


Figure C1. Posterior distribution of the frequencies at $1M_{\odot}$, $1.4M_{\odot}$ and $2M_{\odot}$ for the p_1 -mode. The left panel refers to the prescription described in Sec. 5.3 while the right is obtained by inserting the $R_{\mathbf{X}}(M)$ relation of each model in (14) with the QU coefficients a_i of Sotani (2021). The frequencies in the right panel have a narrower distribution, meaning that the prescription in (16) is necessary to make the spread of our synthetic full GR frequencies similar to the one found by Sotani (2021).

nuclear model dependence can only enter via $\tilde{\Lambda}$, leaving us with the possibility of marginalising over q . For any given instance $\mathcal{M}(\mathbf{X})$:

- (i) From m_c and q we find $m_k(m_c, q)$ for the two NSs, $k = 1, 2$.
- (ii) We can use the model-specific relation $\Lambda_{\mathbf{X}}(M)$: the two tidal deformabilities are $\Lambda_k = \Lambda_{\mathbf{X}}(m_k)$.
- (iii) At this point we can compute $\tilde{\Lambda}_{\mathbf{X}}(q, m_c) = \tilde{\Lambda}(m_k, \Lambda_k)$, where the dependence on $\mathcal{M}(\mathbf{X})$ enters via Λ_k . The arguments of $\tilde{\Lambda}_{\mathbf{X}}$ are q and m_c because of step (i).
- (iv) The likelihood is given by the marginalization over q , namely $\mathcal{L}_{LVC}(\mathbf{X}) \propto \int dq P(\tilde{\Lambda}_{\mathbf{X}}(q, m_c), q)$ over the whole range of possible q values. This is exactly the prescription in (6).

APPENDIX C: TESTING THE PRESCRIPTION FOR THE SYNTHETIC FREQUENCIES

Given a QU relation for the mode frequencies, as the one in (14), it is possible to obtain the mode pulsation $\omega(M)$ simply by using the mass-radius relation $R_{\mathbf{X}}(M)$ of each nuclear model $\mathcal{M}(\mathbf{X})$.

We follow this strategy, using the full GR coefficients of Pradhan et al. (2022) for the f -mode and the ones of Sotani (2021) for the p_1 -mode. As expected, this method works well for the f -mode: we were able to recover the frequency distribution of Pradhan & Chatterjee (2021), as it can be seen in Fig. 5.2. The lower density color map, obtained with the aforementioned method, overlaps with the fit and also the spread of the frequencies is close to the one obtained by Pradhan & Chatterjee (2021).

On the other hand, the p_1 -mode distribution obtained in this way (i.e. by unpacking the QU relation with $R_{\mathbf{X}}(M)$) was narrower than the original spread between the frequencies for different EoS found by Sotani (2021). Hence, we transport the dispersion around the QU relation obtained in Cowling to the full GR prediction, as in Sec. 5.3. In this way, we qualitatively recover the same spread of frequencies reported in Sotani (2021), after we remove the Shen EoS (Shen et al. 1998) used therein, see Fig. C. This EoS is particularly soft and not compatible with the $2.01 M_{\odot}$ observation, consequently it cannot be reproduced by our data.

This paper has been typeset from a $\text{\TeX}/\text{\LaTeX}$ file prepared by the author.